OPTICAL STUDY OF A LOW-SCALE HIGH RADIATIVE FLUX SOLAR FURNACE

Eduardo González-Mora[1], Rasul Akbarov[2] and José D. López Duarte[1]

[1] Facultad de Ingeniería, Universidad Autónoma del Estado de México, Toluca (México)

[2] Institute of Materials Science of Uzbekistan Academy of Sciences, Tashkent (Uzbekistan)

Abstract

Solar concentrators that generate high radiative flux are crucial for advancing sustainable high-temperature research and industrial processes. Solar furnaces achieve this by focusing sunlight using precisely aligned mirrors, enabling applications in materials science and fuel production. However, existing systems are typically large-scale installations, limiting their accessibility for research institutions with spatial constraints. This study addresses the challenge of designing a compact, high-flux solar furnace while retaining high optical performance. Here we demonstrate through Monte Carlo ray-tracing that a faceted parabolic dish, when coupled with a truncated compound elliptic secondary concentrator, achieves a favourable balance of high peak flux (7.2 MW/m^2) and enhanced flux uniformity. Our analysis further reveals that a tailored edge-ray concentrator minimises optical entropy generation, achieving the highest yield despite lower power output. These findings provide a novel framework for optimising secondary concentrator selection based on application-specific requirements for flux intensity versus uniformity. This work establishes a practical foundation for developing efficient, small-scale solar furnaces, potentially expanding access to high-temperature solar research capabilities worldwide. The integration of optical and thermodynamic metrics offers a universally applicable approach for evaluating energy conversion systems across disciplines.

Keywords: Solar furnace, Optical performance, Ray-tracing, Étendue analysis, Entropy generation

1. Introduction

A solar furnace (SF) is an optical device that concentrates solar power to generate high temperatures, enabling applications in materials science, heat treatment, and thermochemical processes such as hydrogen production (Rasul, 2020). Their development involves interdisciplinary studies on optics, solar tracking, and process automation.

Globally, numerous high-temperature research SFs exist in two main configurations: horizontal and vertical axis, as shown in Fig. 1(a) and (b). A third type uses direct sun-tracking with a mobile focal point (Fig. 1(c)). Leading research centres operating such SFs include PROMES (France), PSA (Spain), and DLR (Germany), among others (Riveros-Rosas et al., 2010). The main characteristics of known SFs have been previously catalogued (Shcheglov, 2001), with an updated summary for 2025 provided in Table 1. These systems are often based on mirror concentrators using conical sections, with their characteristics compared in Fig. 2, and find application in processes including steel hardening and nanomaterial synthesis (Fernández-González et al., 2018; Flamant et al., 1999).

However, these facilities are typically large-scale installations, limiting their adoption in space-constrained institutions like ours. The high solar irradiance at our campus in Toluca, México (>500 W/m² DNI for >200 days/year) presents a unique opportunity to develop a compact, small-scale SF capable of reaching high temperatures (Sánchez Pozos, 1997)

To facilitate academic access, we propose a novel compact SF design composed of a heliostat field, a parabolic concentrator, and a nonimaging optics (NIO) component—a strategy known for maximising radiative transfer efficiency. This study focuses on a critical optical analysis of the secondary parabolic concentrator, comparing a continuous surface (theoretical benchmark) with a faceted surface (practical manufacturing feasibility). We evaluate their performance through key parameters such as focal spot size and energy distribution. This work aims to bridge the gap between theoretical optical efficiency and practical construction, advancing the development of efficient, low-cost laboratory solar furnaces (González-Mora and Rincón-Mejía, 2024). Thermal

10.18086/swc.2025.01.14 Available at http://proceedings.ises.org

analysis and sensor measurements are beyond the scope of this initial optical study.

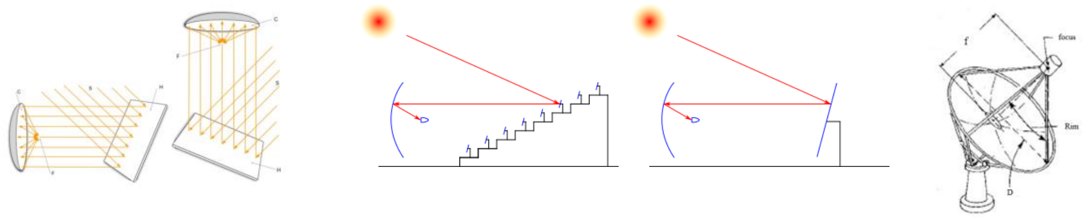

(a) Optical scheme of the solar furnaces with horizontal and vertical axis **(b) Configurations for horizontal axis solar furnaces** **(c) Direct tracking furnace**

Fig. 1. Schematic of solar furnaces (González-Mora and Rincón-Mejía, 2024)**.**

Tab. 1: Data from different solar furnaces around the world. Adapted from (Shcheglov, 2001)**.**

Solar furnace	**Focal concentration ratio**	**Concentrator area, (m^2)**	**Effective diameter, (m)**	**Focal length, (m)**	**Mean focal ratio, (φ)**	**Mean rim-angle, (deg)**	**Overall reflectivity**	**Concentrating efficiency**
NSTFF	4400	35.2	6.7	4.6	1.46	45	0.85	0.158
	3000							0.108
TBS-60	10000		11	6.6	1.67	52	0.86	0.290
HFSF	2500	12.5	3.99	7	0.54	15	0.82	0.660
CNRS-1000	10000	1923	49.5	18	2.75	88	0.7	0.179
CNRS-6.5	6650	13.8	4.2	3.8	1.11	33	-	0.317
	4000							0.263
DGA-45	5800	96	11.06	10.75	1.03	29	-	0.453
PSA	3100	98.5	11.2	7.45	1.50	41	0.83	0.126
PSI	3800	5.7	2.7	1.82	1.48	45	0.57	0.133
WIS	11000	42	7.3	3.75	1.95	53	0.82	0.313
DLR	5200	39.2	7.06	7.3	0.93	26	0.77	0.49
	4800							0.454
UAS	11000	2000	50.46	18	2.8	89	0.70	0.197
IVTAN	5500	57.5	8.55	6.5	1.32	37	0.72	0.276

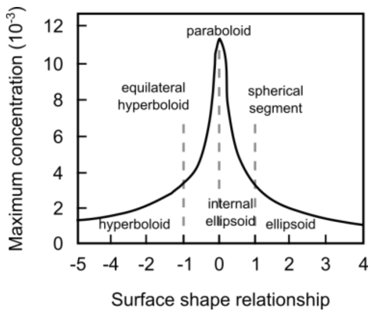

Fig.2. Theoretical concentrating capacity of mirrors of different configurations. Adapted from (Грилихес, 1986).

2. Methodology

The key parameters of the furnace—including its power, focal spot size, concentration ratio, and energy density distribution—are defined by its intended application. These parameters inform the preliminary selection of the system's core components.

This work proposes a small-scale solar furnace inspired by large-scale facilities (LSF), utilising a terrace-arranged heliostat field. In this configuration, flat heliostats (primary mirrors) redirect sunlight to a parabolic concentrator (secondary mirror), which then focuses the radiation onto a nonimaging optics (NIO) component (tertiary stage). This study is deliberately limited to the system's geometric optical design; we defer thermal analysis for future experimental implementation.

2.1. Parabolic mirror and NIO receiver

Flat heliostats in the first optical stage redirect, rather than concentrate, sunlight toward the parabolic mirror. The parabolic dish (PD) and the subsequent NIO stage together achieve concentration, as described by

$$C_g = \prod_i C_{g_i} = C_{g_{PD}} C_{g_{NIO}} \qquad \text{(eq. 1)}$$

The parabolic geometry's cross-section (Fig. 3a) allows determination of the maximum geometric concentration (Eq. 2) by considering receiver shading, the rim angle θ_r, and the acceptance semi-angle θ_0. his concentration yields a maximum concentration of 11433 for $\theta_0 = 16'$ and $\theta_r = 44.86°$.

$$C_{g_{PD}} = \frac{\sin^2\theta_r \cos^2(\theta_r+\theta_0)}{\sin^2\theta_0} - 1 \qquad \text{(eq. 2)}$$

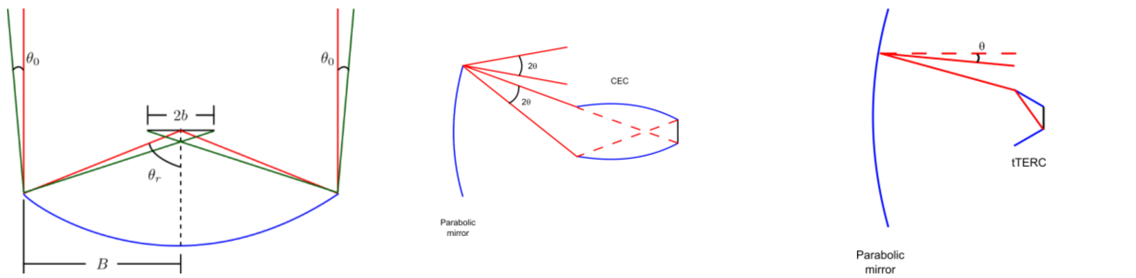

(a) Parabolic mirror **(b) Compound elliptic concentrator (CEC)** **(c) Truncated tailored edge ray concentrator (tTERC)**

Fig. 4. Optical geometries for the solar furnace.

The total geometric concentration depends heavily on the secondary NIO stage, which can use mirrors or lenses. Coupling a second stage requires adjusting the acceptance angle; for mirrors, it becomes $\theta_0' = \theta_r + \theta_0$, while for lenses, it is governed by Snell's law ($n \sin\theta_0' = \sin(\theta_r + \theta_0)$), though lens melting is a significant concern. Compound elliptical concentrators (CEC) and truncated tailored edge ray concentrators (tTERC) are the most suitable NIO geometries for solar furnaces (Figs. 4b and 4c). Their concentration ratio is:

$$\begin{cases} C_{g_{CEC}} = \frac{1}{\sin^2(\theta_r+\theta_0)} \\ C_{g_{tTERC}} = 4\cos^2(\theta_r+\theta_0) + 1 \end{cases} \qquad \text{(eq. 3)}$$

Equation 4 defines the total system concentration, which Fig. 5 depicts using the normalised ratio $C_g^* = C_{g_x}/C_{g_{max}}$ (where $C_{g_{max}} = 1/\sin^2\theta_0$). This plot shows that two rim angle (θ_r) solutions exist for a given concentration ratio. The aperture-to-focal distance parameter guides the optimal choice, φ (Eq. 5).

$$C_{g,tot} = \begin{cases} \left(\frac{\sin^2\theta_r\cos^2(\theta_r+\theta_0)}{\sin^2\theta_0} - 1\right)\left(\frac{1}{\sin^2(\theta_r+\theta_0)}\right) & \text{for PD + CEC} \\ \left(\frac{\sin^2\theta_r\cos^2(\theta_r+\theta_0)}{\sin^2\theta_0} - 1\right)(4\cos^2(\theta_r+\theta_0)+1) & \text{for PD + tTERC} \end{cases} \quad \text{(eq. 4)}$$

$$\varphi = \frac{A_{ap}}{f} \quad \text{(eq. 5)}$$

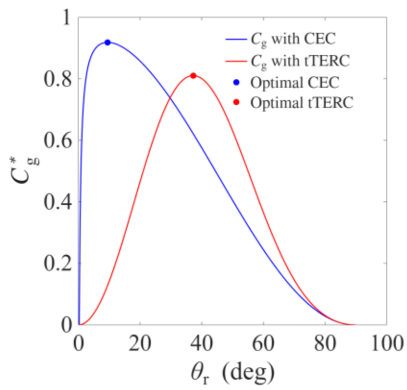

Fig. 5. Normalized concentration ratio for the two NIO configurations with the parabolic mirror.

Rays incident on the parabolic concentrator at a high angle of incidence are optically inefficient. This effect, which corresponds to zones with a large rim angle, is quantified by the cosine factor; its significant decrease beyond 45° led us to select 60° as a practical upper limit for the rim angle. For this design, we fix an aperture diameter $2B = 2$ m and a half-acceptance angle $\theta_0 = 0.5°$. This configuration yields a focal length of $f = 0.866$ m and an aperture-to-focal distance parameter $\varphi = 2.31$. Under these conditions, the tTERC system achieves a total geometric concentration ratio ($C_{g,tot}$) of 4920, compared to 3151 for the CEC system.

Based on these parameters, we evaluated two parabolic reflector configurations: an ideal continuous surface, which provides a theoretical efficiency benchmark by perfectly focusing all rays, and a practical faceted design using hexagonal segments. While the faceted approach incurs efficiency losses from segmentation and misalignment, it enables the furnace's physical construction.

Faceting procedure

We discretised the continuous parabolic surface into flat hexagonal facets using a systematic coordinate generation process. We selected a fixed facet side length of $s = 10$ cm to balance optical precision with manufacturing constraints. One can then calculate the facet apothem as $a = s\sqrt{3}/2$. The maximum expansion level $L_{max} = \lfloor B/s\sqrt{3} \rfloor$ where $B = 1$ m is the half aperture, determines the number of concentric hexagonal layers. The algorithm generates facet centres level by level: Level 0 places a central facet at the origin (0,0), while subsequent levels $L = 1$ to L_{max} position facets using axial coordinate formulas $(x_c, y_c) = \left(3s/2q, s\sqrt{3}(r + q/2)\right)$, for integer indices $q \in [-L, L]$ and $r \in [\max(-L, -q-L), \min(L, -q+L)]$, retaining only those facets satisfying $\sqrt{x_c^2 + y_c^2} \leq B$. The resulting 2D coordinates are mapped onto the parabolic surface via $z_c = (x_c^2 + y_c^2)/4p$ to approximate the curvature. This process generated 91 contiguous hexagonal facets arranged in a non-overlapping honeycomb lattice fully covering the dish aperture, as shown in Fig. 6. Finally, we derived the surface normal vector $\underline{\hat{n}}$ for each facet using Snell' law: $\underline{\hat{n}} = (\underline{\hat{s}} + \underline{\hat{r}})/\|\underline{\hat{s}} + \underline{\hat{r}}\|$ where $\underline{\hat{s}} = (0,0,1)$ is the solar beam direction and $\underline{\hat{r}} = \left(\underline{f} - \underline{P}\right) / \left\|\underline{f} - \underline{P}\right\|$ is the unit vector from the facet centre $\underline{P} = (x_c, y_c, z_c)$ to the focus $\underline{f} = (0,0,f)$.

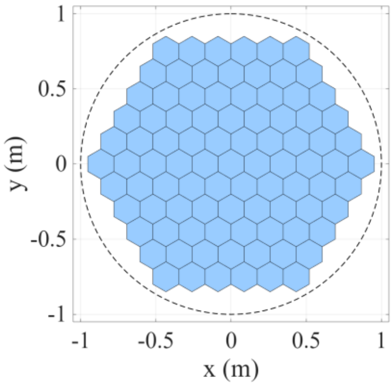

Fig. 6. Schematic representation of the parabolic surface faceting.

2.2. Heliostat field layout

Given the established parabolic mirror dimensions and inspired by the Large Solar Furnace (LSF) in Uzbekistan (Rasul, 2020), the heliostat field will be arranged across eight terraces with a 45-degree slope. Each terrace will hold eight square, flat heliostats measuring 24 cm × 24 cm, resulting in a total of 64 identical single-facet mirrors. The spatial distribution of this heliostat field, including side and top views, is illustrated in Fig. 7. The implementation of the sun-tracking system falls outside the scope of this optical design study; we will address this challenge in future work.

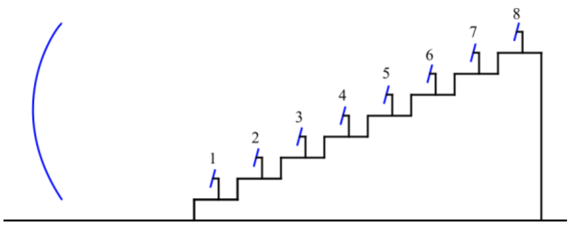

(a) Side view of the heliostat field array.

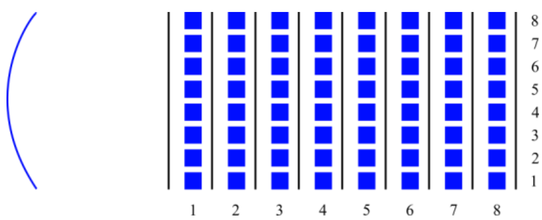

(b) Top view of the heliostat field array.

Fig. 7. Heliostat field layout.

2.3 Material selection and properties

The selection of optical materials is paramount for reconciling optical efficiency against practical manufacturing constraints and cost. The geometric requirement of segmenting the primary parabolic reflector into small hexagonal facets (10 cm per side) necessitates a material amenable to precision cutting and shaping while maintaining high reflectivity. Although thin-glass solar mirrors are an option, high-reflective aluminium sheets offer a compelling alternative due to their excellent workability, competitive optical performance, and durability. Both the secondary parabolic surface and the tertiary concentrator (CEC or tTERC) utilise the same reflective material—commercial aluminium reflector (ALANOD, 2024), with an average reflectivity of 0.9, to prevent efficiency losses associated with material mismatches. This choice strategically balances high optical performance with practical manufacturability.

We modelled optical errors using conservative worst-case parameters from Klychev et al. (2024). A specularity error ($\sigma_{specular}$) of 2.327 mrad and a slope error (σ_{slope}) of 1.164 mrad were applied uniformly across all ray-tracing simulations to establish a performance boundary under consistent optical imperfections, providing a baseline for error sensitivity analysis.

2.4 Ray-tracing procedure

Monte Carlo ray-tracing (MCRT) is a statistical simulation method for modelling light transport in complex optical systems. SolTrace (Wendelin, 2003), a specialised MCRT tool, is widely used in solar energy applications. It works by stochastically generating millions of rays from a light source, such as the sun, and then probabilistically modelling their interactions (reflection, refraction, scattering) with surfaces. The statistical averaging of these ray paths provides solutions for flux distributions and efficiency metrics, with the uncertainty decreasing as the number of rays increases.

To validate the results of the ray-tracing simulations for the solar furnace, we employ the well-known empirical Aparisi formula (Zakhidov et al., 1992) as a benchmark for the PD stage. This formula provides a practical method for calculating the energy distribution in the focal region of a parabolic concentrator and takes the following form:

$$\dot{Q}_r = G_{bn}\rho h^2 \sin^2\theta_r\, e^{-cr^2} \quad \text{(eq. 7)}$$

where $c = (h/2f)^2(1+\cos\theta_r)^2$, G_{bn} is the beam radiation, ρ is the mirror reflectivity, r is the distance along the longitudinal section and $h = (180/\pi)\sqrt{\mathrm{erf}(\theta_s/\sqrt{2}\sigma_{tot})}$ is a measure of the concentrator accuracy, according to Poluektov and Grilikhes (1967), with σ_{tot} as the total optical error. Two main approaches define the total optical error: the numerical integration of images from real systems, or the error behaviour treatment as a Gaussian distribution (Duffie and Beckman, 2013). For focusing concentrators, the Gaussian approach is well-justified. Since the Aparisi's equation considered the Gaussian behaviour, we can rely on the Gaussian description given by (1985):

$$\sigma_{tot}^2 = 4\sigma_{slope}^2 + \sigma_{specular}^2 + \sigma_{sun}^2 \quad \text{(eq. 7)}$$

2.5 Étendue analysis

To incorporate the effects of optical irreversibility, we include the entropy generation from étendue loss in the total entropy balance. Following the approach of González-Mora and Rincón-Mejía (2023), the entropy change from optical dispersion is given by $\dot{S}_{gen}^{\varepsilon sc} = \dot{N}k\ln(1+\varepsilon_{sc}^*)$, where $\dot{N} = \dot{Q}_s/E_{ph}$ is the photon flux, $\dot{Q}_s$ is the net solar energy input, $E_{ph} \approx 10^{-19}$ J is the average photon energy, k is Boltzmann's constant, and $\varepsilon_{sc}^* = (\varepsilon_{out} - \varepsilon_{in})/\varepsilon_{in}$ is the dimensionless étendue spillage factor. This optical entropy term complements thermal irreversibility, yielding the total entropy generation $\dot{S}_{gen}^{total} = \dot{S}_{gen}^{\varepsilon sc} + \dot{S}_{gen}^{th}$.

A dimensionless parameter ψ (Eq. 9) quantifies the relative contribution of étendue spillage to overall irreversibility. As shown by González-Mora and Rincón-Mejía (2023), ψ approaches 1 when optical losses dominate and 0 when thermal irreversibility prevails, providing a valuable metric for evaluating optical quality.

$$\psi = \frac{\dot{S}_{gen}^{\varepsilon sc}}{\dot{S}_{gen}^{total}} \quad \text{(eq. 9)}$$

3. Results

We evaluate the optical performance of the high-flux solar furnace system through a series of ray-tracing simulations. The system was defined by a 2 m diameter parabolic dish (PD) with a 60° rim angle and a 0.5° acceptance angle, yielding a focal length of 0.866 m and a focal spot diameter of 0.0409 m. This study simulated a total of six arrangements by combining two secondary concentrators—a compound elliptic concentrator (CEC, in both full and truncated form) and a truncated tailored edge-ray concentrator (tTERC)—with two primary reflector surface types (continuous and faceted). All configurations maintained a fixed 60.5° acceptance angle and received illumination from a field of 64 heliostats. The resulting receiver diameters were 0.0356 m for the CEC and 0.0285 m for the tTERC, producing total geometric concentration ratios of 3151.2 and 4920.0, respectively. This section details the validation of the simulation methodology and discusses the key performance metrics for these configurations.

3.1 Validation of ray-tracing convergence

A critical prerequisite for analysing the simulation results is establishing the statistical reliability of the ray-tracing data. We rigorously verify the convergence of the Monte Carlo ray-tracing algorithm for each optical configuration. The analysis focused on five key parameters: peak flux, peak flux uncertainty, average flux, average flux uncertainty, and total power transmitted to the receiver. A plot of parameter uncertainty against the inverse square root of the number of rays launched ($N^{-1/2}$) confirmed valid convergence for all parameters, as evidenced by the establishment of a straight-line relationship for each (Fig. 8). This multi-parameter convergence check ensures the robustness and statistical significance of all subsequent results.

Following convergence validation, we benchmarked the entire ray-tracing procedure against a known theoretical model. Figure 9 presents a comparison between the theoretical Aparisi flux profile for the parabolic dish and the flux profile retrieved directly from the SolTrace simulation of the heliostat field and parabolic dish (without any secondary concentrator). The strong agreement between the two profiles confirms two critical points: first, the chosen ray-tracing validation criterion is adequate for this optical system, and second, the implementation and considerations within the SolTrace environment are correct. This validation provides high confidence in the model's ability to accurately simulate the optical behaviour of the complete system, including the heliostat field, parabolic dish, and secondary concentrators.

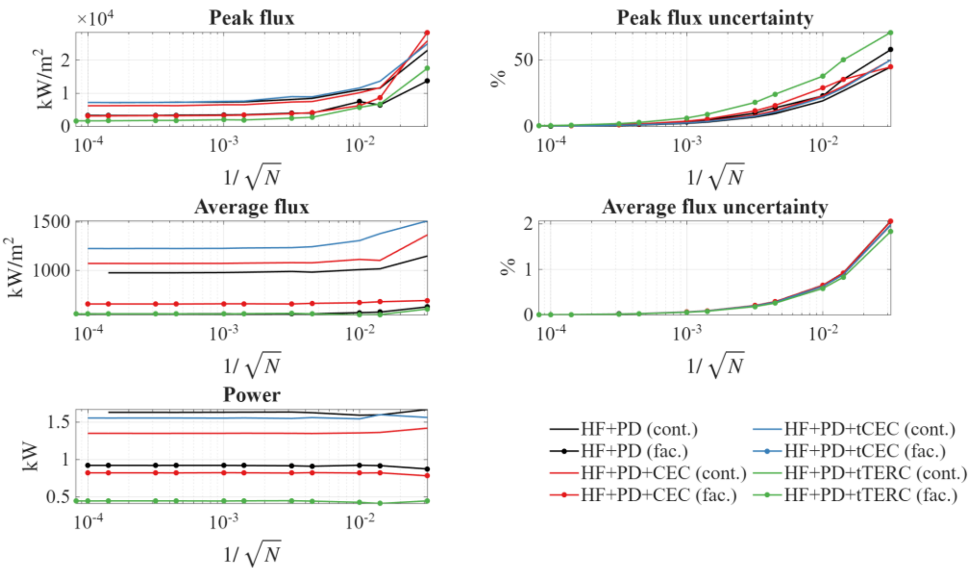

Fig. 8. Ray-tracing convergence.

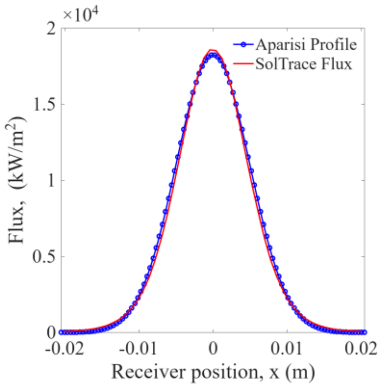

Fig. 9. Comparison of the flux profile in the receiver between the Aparisi's equation and SolTrace.

3.2 Optical performance of the solar furnace

Figure 10 presents the flux profiles at the final receiver for the complete optical systems, and Table 2 compiles the corresponding quantitative data for all configurations. The results reveal significant performance variations based on the secondary concentrator type and the primary reflector's surface finish (continuous vs. faceted).

A consistent trend across all eight configurations is the reduced performance of the faceted parabolic surface compared to its continuous counterpart. We expected this result, as faceting introduces microscopic aberrations that scatter rays, causing a portion of the concentrated flux to miss the intended receiver target. Consequently, every faceted configuration exhibits a systematic reduction in peak flux, average flux, and total transmitted power.kW/m^2

The choice of the secondary concentrator greatly influences the flux distribution. The system incorporating the tTERC exhibits the most pronounced effect, as it attenuates the peak flux by a factor of four compared to the PD-only case, while also lowering the average flux and total power. This significant flattening of the flux profile, as clearly seen in Fig. 10, indicates a high degree of uniformity. This result makes the tTERC configuration particularly advantageous for applications requiring uniform heating, such as specific thermochemical processes or material testing, where hot spots are detrimental.

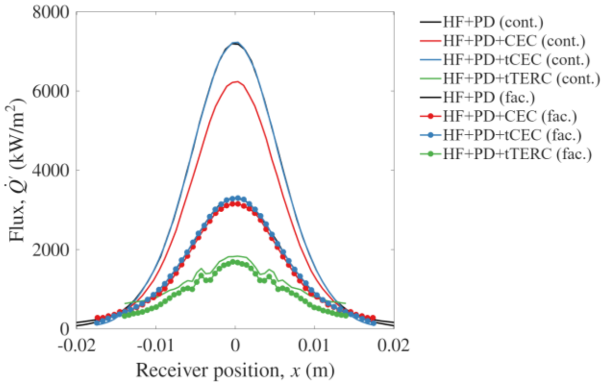

Fig. 10. HFSF configurations receiver' flux profiles.

Table 2: Power characteristics of the analysed configurations.

Parameter	**Heliostats + PD**		**Heliostats + PD + full CEC**		**Heliostats + PD + truncated CEC**		**Heliostats + PD + tTERC**	
	Contin-uous	**Fac-eted**	**Continu-ous**	**Faceted**	**Continu-ous**	**Faceted**	**Contin-uous**	**Faceted**
Peak flux (kW/m^2)	7193.25	3314.83	6236.25	3167.11	7236.21	3324.99	1863.9	1683.14
Average flux (kW/m^2)	975.08	551.39	1071.73	652.81	1226.19	674.02	729.59	550.98
Power (kW)	1.631	0.922	1.351	0.823	1.555	0.855	0.592	0.448
ψ number (10^5)	7.147	7.222	7.278	7.353	7.278	7.353	6.860	7.201

The integration of a full CEC presents a different trade-off. It results in a moderate decrease in peak flux and total power but a notable increase in the average flux on the receiver compared to the PD-only case. This combination of a lower peak-to-average ratio indicates an improvement in flux uniformity. This behaviour is consistent for both continuous and faceted primary surfaces, suggesting that the CEC effectively homogenises the flux distribution at the cost of some peak concentration.

Conversely, the truncated CEC configuration demonstrates a unique and beneficial performance. It achieves a higher peak flux and a significantly higher average flux than both the PD-only and full CEC cases. This result indicates that truncation mitigates some optical losses inherent in the full CEC design, making it the most effective concentrator for maximising the intensity of incident radiation while still improving uniformity over the PD-only case.

We extended the performance analysis beyond flux and power metrics to include a dimensionless thermodynamic evaluation of optical irreversibility using the dimensionless ψ parameter. As shown in Table 2, the ψ values for all configurations are on the order of 10^{-5}, indicating that thermal irreversibility is the dominant loss mechanism in this system. However, the subtle variations between configurations provide valuable insight. The tTERC with a continuous surface yields the lowest ψ value (6.860×10^{-5}), consistent with its design principle of minimising optical entropy generation through tailored edge-rays. This result confirms its superior optical quality from a thermodynamic perspective, even though it delivers lower power. Conversely, the faceted configurations consistently show slightly higher ψ values than their continuous counterparts, corroborating the finding that surface faceting increases optical losses and étendue spillage. The values for the CEC configurations fall between these extremes, with the truncated and full versions performing identically in terms of entropy generation, suggesting their étendue-spilling characteristics are similar despite their different flux-shaping effects.

A key observation from these results is that the addition of a secondary concentrator does not drastically increase the system's total concentration ratio. Instead, its primary function is to reshape the flux distribution incident from the parabolic dish. The full CEC and tTERC primarily enhance uniformity, while the truncated CEC offers a valuable compromise, boosting both peak and average flux. The thermodynamic analysis further reveals that the tTERC achieves this flux homogenisation with the highest optical yield (lowest (lowest ψ). This finding suggests that the primary benefit of these secondary elements lies in tailoring the thermal profile for specific applications rather than in mere concentration amplification. Therefore, future work should focus on a parametric optimisation of the optical system (e.g., varying the parabolic dish's rim angle or the secondary concentrator's acceptance angle) to custom-design flux profiles that minimise total entropy generation (ψ) for targeted high-temperature processes.

4. Conclusions

This study aimed to design and optically characterise a novel, compact high-flux solar furnace, evaluating the performance of a parabolic dish concentrator when coupled with various nonimaging secondary concentrators. We employed a Monte Carlo ray-tracing methodology in SolTrace, validated against established theoretical models, to compare ideal continuous surfaces with practical faceted surfaces under realistic optical error parameters. Our analysis extended beyond conventional flux metrics to include a thermodynamic assessment of optical irreversibility using the dimensionless ψ parameter.

The simulations demonstrated that while faceting the primary reflector introduces predictable optical losses, the choice of secondary concentrator primarily governs the system's flux profile. The truncated compound elliptic concentrator emerged as the most effective compromise, uniquely enhancing both peak and average flux intensity. Conversely, the tailored edge-ray concentrator achieved superior flux uniformity and the lowest entropy generation, signifying higher optical quality. The study reveals that the primary function of these secondary elements is not significant concentration amplification, but the strategic tailoring of the thermal profile to address application-specific requirements.

A key limitation of this work is its exclusive focus on optical performance at a fixed solar noon configuration; thermal analysis and performance under varying solar angles remain critical for a complete system evaluation. Furthermore, the manufacturing and alignment tolerances for the faceted design, though considered, require empirical verification.

These findings represent a significant advancement in the design of small-scale solar furnaces, demonstrating a quantitative link between optical configuration and both radiative and thermodynamic performance. The results indicate that a faceted primary reflector is a viable, cost-effective strategy that avoids performance loss, thereby enabling wider adoption in resource-constrained settings. The ψ parameter proved to be a valuable metric for evaluating optical yield, offering a new dimension for comparing concentrator designs beyond concentration ratio alone.

Future research should focus on a parametric optimisation of the system, investigating the influence of the rim angle and acceptance angle on both the flux distribution and the total entropy generation. Subsequent work must also validate these optical models through experimental construction and testing, integrating sun-tracking and thermal analysis to assess performance under real operating conditions. This study establishes a robust optical foundation for developing efficient, small-scale solar furnaces suitable for advanced materials research and thermochemical processing.

5. Acknowledgments

This work was partially funded by COMECyT grant CAT2024-0112 (AESCo project), which supported Eduardo González-Mora through the *Programa Investigadoras e Investigadores*.

6. References

ALANOD, 2024. Product Data Sheet 8510GP. Ennepetal.

Duffie, J.A., Beckman, W.A., 2013. Solar Engineering of Thermal Processes, 4th ed. John Wiley & Sons, Inc.

Fernández-González, D., Ruiz-Bustinza, I., González-Gasca, C., Piñuela Noval, J., Mochón-Castaños, J., Sancho-Gorostiaga, J., Verdeja, L.F., 2018. Concentrated solar energy applications in materials science and metallurgy. Solar Energy 170, 520–540. https://doi.org/10.1016/j.solener.2018.05.065

Flamant, G., Ferriere, A., Laplaze, D., Monty, C., 1999. SOLAR PROCESSING OF MATERIALS: OPPORTUNITIES AND NEW FRONTIERS. Solar Energy 66, 117–132. https://doi.org/10.1016/S0038-092X(98)00112-1

González-Mora, E., Rincón-Mejía, E.A., 2024. Diseño de un horno solar de alto flujo de baja escala, in: Horta, P. (Ed.), XIX Congreso Ibérico y XV Congreso Iberoamericano de Energía Solar. Évora.

González-Mora, E., Rincón-Mejía, E.A., 2023. A Simple Truncation Criterion in CPCs Using Constructal Theory, in: 36th International Conference on Efficiency, Cost, Optimization, Simulation and Environmental Impact of Energy Systems (ECOS 2023). ECOS 2023, Las Palmas De Gran Canaria, Spain, pp. 1678–1688. https://doi.org/10.52202/069564-0152

Klychev, Sh.I., Bakhramov, S.A., Parpiev, O.R., Paizullakhanov, M.S., Suvonova, L.S., Kadyrgulov, D.E., Matjanov, E.K., Giyasova, F.A., 2024. Optical-Energy Characteristics and Heating Temperatures in Small Single-Mirror Solar Furnaces. Applied Solar Energy 60, 703–707. https://doi.org/10.3103/S0003701X24602394

Poluektov, V.P., Grilikhes, V.A., 1967. Determining the characteristics of the radiation field in the focal plane of parabolic solar concentrators 4:6.

Rabl, A., 1985. Active Solar Collectors and Their Applications. Oxford University Press.

Rasul, A., 2020. Thousand kW High-Temperature Solar Furnace in Parkent (Uzbekistan) – Energetical Characteristics, in: A Guide to Small-Scale Energy Harvesting Techniques. IntechOpen. https://doi.org/10.5772/intechopen.83411

Riveros-Rosas, D., Herrera-Vázquez, J., Pérez-Rábago, C.A., Arancibia-Bulnes, C.A., Vázquez-Montiel, S., Sánchez-González, M., Granados-Agustín, F., Jaramillo, O.A., Estrada, C.A., 2010. Optical design of a high radiative flux solar furnace for Mexico. Solar Energy 84, 792–800. https://doi.org/10.1016/j.solener.2010.02.002

Sánchez Pozos, M., 1997. Desarrollo de un colector experimental de ultra concentración solar. Universidad Autónoma del Estado de México.

Shcheglov, V., 2001. Comparative analysis of the solar furnaces performances. Geliotechnika 2.

Wendelin, T., 2003. SolTRACE: A New Optical Modeling Tool for Concentrating Solar Optics, in: Solar Energy. ASMEDC, pp. 253–260. https://doi.org/10.1115/ISEC2003-44090

Zakhidov, R.A., Weiner, A.A., Umarov, G.I., 1992. Theory and Calculation of Applied Solar Energy Concentrating Systems. Gujarat Energy Development Agency.

Грилихес, В.А., 1986. Солнечные космические энергостанции. Наука.